The Astrophysical Journal, 834:150 (11pp), 2017 January 10 doi:10.3847/1538-4357/834/2/150

A STATISTICAL STUDY OF FLARE PRODUCTIVITY ASSOCIATED WITH SUNSPOT PROPERTIES IN DIFFERENT MAGNETIC TYPES OF ACTIVE REGIONS

Ya-Hui Yang[1], Min-Shiu Hsieh[2], Hsiu-Shan Yu[3], and P. F. Chen[4]
[1] Institute of Space Science, National Central University, Jhongli 32001, Taiwan; yhyang@jupiter.ss.ncu.edu.tw
[2] Geophysical Institute, University of Alaska Fairbanks, AK 99775-7320, USA; mhsieh2@alaska.edu
[3] Center for Astrophysics and Space Sciences, University of California San Diego, CA 92093, USA; hsyu@ucsd.edu
[4] School of Astronomy & Space Science, Nanjing University, Nanjing 210023, China; chenpf@nju.edu.cn
Received 2016 May 20; revised 2016 November 20; accepted 2016 November 21; published 2017 January 11

ABSTRACT

It is often believed that intense flares preferentially originate from the large-size active regions (ARs) with strong magnetic fields and complex magnetic configurations. This work investigates the dependence of flare activity on the AR properties and clarifies the influence of AR magnetic parameters on the flare productivity, based on two data sets of daily sunspot and flare information as well as the *GOES* soft X-ray measurements and HMI vector magnetograms. By considering the evolution of magnetic complexity, we find that flare behaviors are quite different in the short- and long-lived complex ARs and the ARs with more complex magnetic configurations are likely to host more impulsive and intense flares. Furthermore, we investigate several magnetic quantities and perform the two-sample Kolmogorov–Smirnov test to examine the similarity/difference between two populations in different types of ARs. Our results demonstrate that the total source field strength on the photosphere has a good correlation with the flare activity in complex ARs. It is noted that intense flares tend to occur at the regions of strong source field in combination with an intermediate field-weighted shear angle. This result implies that the magnetic free energy provided by a complex AR could be high enough to trigger a flare eruption even with a moderate magnetic shear on the photosphere. We thus suggest that the magnetic free energy represented by the source field rather than the photospheric magnetic complexity is a better quantity to characterize the flare productivity of an AR, especially for the occurrence of intense flares.

Key words: Sun: flares – Sun: magnetic fields – sunspots

1. INTRODUCTION

Solar flares are commonly observed at the active regions (ARs) with different magnetic field complexities. Associations between flare productivity and AR properties have been discussed extensively in previous studies (e.g., Giovanelli 1939; Greatrix 1963; Sammis et al. 2000; Lee et al. 2012; He et al. 2014). It is generally believed that intense flares preferentially originate from the ARs containing large sunspot groups with strong magnetic fields and complex magnetic field configurations. To characterize their complexity, sunspot groups are classified into eight types with an ascending order, i.e., α, β, γ, $\beta\gamma$, δ, $\beta\delta$, $\beta\gamma\delta$, and $\gamma\delta$, according to the Mount Wilson magnetic classification. Earlier studies indicated that the δ-type sunspot groups, in which two umbrae with opposite magnetic polarities are embedded in one penumbra, are highly related to the major flare eruptions (Atac 1987; Zirin & Liggett 1987). Mayfield & Lawrence (1985) found that the δ-type ARs are likely efficient for flare productions.

Shi & Wang (1994) reported that 96% of X-class flares erupt from the ARs with δ-type sunspots in solar cycle 22 and the productivity of X-class flares is closely correlated to the lifetime of δ sunspots. However, only 23% of their studied δ sunspots produced X-class flares during the disk passages. Sammis et al. (2000) showed that the ARs classified as the $\beta\gamma\delta$ type tend to produce stronger flares compared to other types of ARs with similar sizes. They found that the $\beta\gamma\delta$ sunspots with area greater than 1000 millionths of the solar hemisphere (μHem) have a 40% probability of producing X-class flares. Subsequently, Chen et al. (2011) selected 45 super-ARs based on the maximum sunspot area, the flare index, the 10.7 cm radio peak flux, and the variation in total solar irradiance. They demonstrated that these regions can produce 44% of X-class flares during solar cycles 21–23. Guo et al. (2014) showed that 88% of X-class flares occur in the $\beta\gamma\delta$ sunspot regions during the period of solar cycles 22–23. Takizawa & Kitai (2015) revealed that more complex ARs have a longer δ-state, and that the flare index and the δ-state duration are positively correlated.

In addition to the morphological classification of sunspot groups, quantifying the magnetic nonpotentiality would be more helpful for understanding the flare productivity of ARs. The relationship between magnetic nonpotentiality and flare productivity can be characterized by several physical parameters deduced from the photospheric magnetic fields, for instance, the magnetic shear (e.g., Hagyard et al. 1984; Wang et al. 1996; Tian et al. 2002; Cui et al. 2007; Leka & Barnes 2007; Tiwari et al. 2010; Yang et al. 2012), the source field (e.g., Wang et al. 1996; Yang et al. 2014), and the magnetic free energy (e.g., Leka & Barnes 2007; Jing et al. 2010; Chen & Wang 2012; Yang et al. 2012; Su et al. 2014). It was noted that flare-productive ARs cannot be distinguished from flare-quiet ARs by only considering one specific parameter (Leka & Barnes 2003). Among various proxies, the photospheric magnetic free energy was found to be a relatively good parameter to differentiate between the flare-productive and the flare-quiet ARs for intense flares, i.e., M- and X-class events (Leka & Barnes 2007). Additionally, it was found that the complex ARs with larger flux imbalance between two opposite polarities are more associated with major flares (Shi & Wang 1994; Tian et al. 2002; Romano & Zuccarello 2007; Chen & Wang 2012).

Although many efforts have been carried out, the major physical quantity that best characterizes the correlation between the AR properties and flare activity in different types of ARs is still unclear. In this study, we address the dependence of flare magnitude on AR properties during the period of 1996–2014 for which the time evolution of AR profiles is considered. We also clarify the significance of magnetic parameters on flare productivity using the high-resolution vector magnetograms from the Helioseismic and Magnetic Imager (HMI; Scherrer et al. 2012; Schou et al. 2012) on board the *Solar Dynamic Observatory* (*SDO*) during 2010–2014. In addition, we compare several photospheric quantities, such as the magnetic field strength, total magnetic flux, flux imbalance, magnetic shear, and source field strength between those ARs with simple and complex magnetic configurations, as well as between the flaring and flare-quiet ARs. The data sets and categories used in this study are briefly introduced in Section 2. In Section 3 we present the dependence of flare activities on the ARs with different magnetic types. We finally provide discussions and conclusions in Sections 4 and 5, respectively.

2. DATA REDUCTION

Two categories of data sets from 1996 to 2014 are utilized for the event selection in this study. One is the daily sunspot information, including the region number, the location, the area, and the magnetic type. This data set is obtained from the Joint USAF/NOAA Solar Region Summary.[5] We use the Mount Wilson magnetic classification to identify the magnetic type of an AR. For simplicity, all the ARs are classified into three groups, that is, simple type (i.e., α, β, or γ), intermediate type (i.e., $\beta\gamma$, δ, or $\beta\delta$), and complex type (i.e., $\beta\gamma\delta$ or $\gamma\delta$), from the low to high magnetic complexity based on the most complex magnetic type during the disk passage of each AR. The lifetime T_i of an AR with the highest magnetic complexity and the corresponding appearance date D_i are recorded. Here the subscript i is "sim," "int," or "com," corresponding to the simple, intermediate, or complex ARs, respectively.

The second data set is the daily solar flare information from the *GOES* X-ray event lists provided by GSFC/NASA,[6] where the flare magnitude, time, and corresponding AR number and position are recorded. The recurrent sunspot group turning from the backside of the Sun is assigned to a new NOAA AR number in its second disk transit and is thus regarded as a different AR here. In this study, the flare duration is estimated from the difference between flare start time and end time recorded in the event list. The *GOES* soft X-ray (SXR) flux in the 1–8 Å wavelength with 3 s average is utilized to calculate the physical quantities associated with the flare magnitude. For example, the SXR fluence F_t is derived by integrating the SXR flux from the flare start time to the end time. Note that only those regions recorded in both sunspot and flare data sets with nonzero sunspot areas are taken into account in our database.

In addition, the HMI vector magnetograms during 2010–2014 and the potential field model are employed to derive the photospheric magnetic properties. One kind of HMI data product called space-weather HMI active region patches (SHARPs) provides the processed and cutout images with a 720 s cadence, which is appropriate for investigating the AR properties as well as its evolution. The cylindrical equal-area (CEA) data set of the SHARPs is used in this study, where all quantities are remapped to a heliographic CEA projection centered on the patch. The photospheric magnetic field components provided by the CEA data set are the radial, latitudinal, and longitudinal magnetic fields (B_r, B_θ, and B_ϕ) in the heliographic spherical coordinates. The physical size of one pixel in the CEA map is 360 km. For more information on the SHARP data series and the associated coordinate system, readers can refer to Sun (2013) and Bobra et al. (2014).

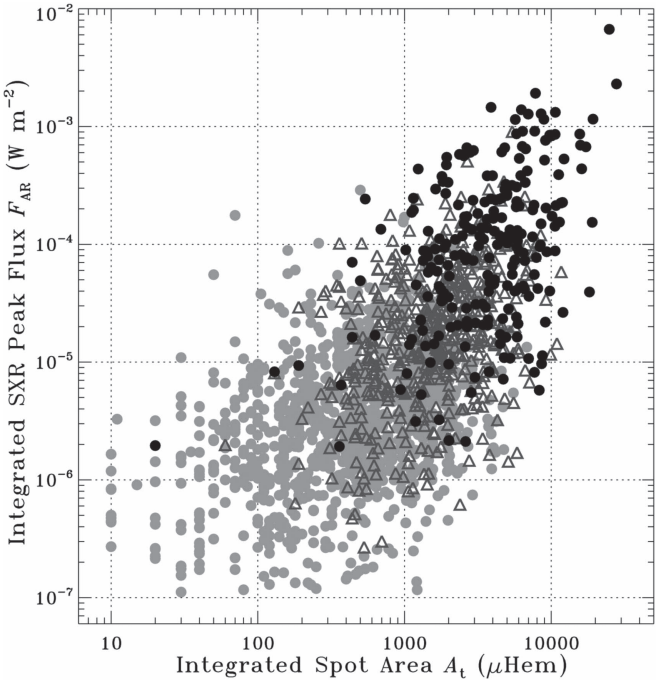

Figure 1. Associations between the integrated SXR peak flux and the integrated spot area in all ARs. The dark circles, triangles, and gray circles represent the complex, intermediate, and simple types of ARs, respectively.

3. RESULTS

3.1. Sunspot Properties versus Flare Occurrence

In this section we examine the general properties of sunspot regions in association with flare magnitude and productivity. The AR capability of flare production is represented by F_{AR}, which is similar to the flare index and is derived by integrating the SXR peak flux of all flare events larger than B-class during the disk transit of an AR. The integrated spot area A_t summing up all the daily sunspot areas recorded during an AR's disk passage is used to represent the evolution pattern of AR size. Figure 1 demonstrates the correlation between F_{AR} and A_t in all the analyzed ARs, where the dark circles, triangles, and gray circles represent the complex, intermediate, and simple types of ARs, respectively. It is shown that F_{AR} is positively related to A_t, which is consistent with the results found by Sammis et al. (2000). However, some simple ARs can host intense flares (e.g., $F_{AR} > 10^{-4}\,\mathrm{W\,m^{-2}}$) or some complex ARs would produce small flares (e.g., $F_{AR} < 5 \times 10^{-6}\,\mathrm{W\,m^{-2}}$).

To investigate the detailed flare properties in association with different magnetic types of ARs, the flare events are divided into nine divisions based on three kinds of magnetic complexity and three regimes of SXR fluence F_t. Regimes 1, 2, and 3 correspond to $F_t \geqq 10^{-2}\,\mathrm{J\,m^{-2}}$, $10^{-3} \leqq F_t < 10^{-2}\,\mathrm{J\,m^{-2}}$, and $F_t < 10^{-3}\,\mathrm{J\,m^{-2}}$, respectively. Here we use the two-sample

[5] http://legacy-www.swpc.noaa.gov/ftpmenu/warehouse.html
[6] ftp://hesperia.gsfc.nasa.gov/goes/goes_event_listings

Kolmogorov–Smirnov (KS) test to measure the similarity or difference between any two populations of ARs. We examine the cumulative distribution function (CDF) for the flare duration and flare magnitude in each regime. The statistic of the two-sample KS test, K, is defined by the maximum vertical deviation between two population curves; that is, the larger $K_{com,sim}$ value corresponds to the larger difference of properties between the complex and simple ARs. Figure 2 demonstrates the result of the two-sample KS test in the complex (dark) and simple (gray) ARs, where the statistic $K_{com,sim}$ is indicated by the dotted line. It is shown that the maximum $K_{com,sim}$ is in regime 3, i.e., the weakest F_t. Figure 2 also shows that in the same F_t regime, the flares erupted from the complex ARs have shorter duration and stronger magnitude compared to the flares from the simple ARs. This implies that the ARs with complex magnetic configurations are likely associated with the impulsive and intense flares. In comparison, we analyze the CDF curves between intermediate and simple types of ARs as well as the CDF curves between complex and intermediate types of ARs (not shown here). The result that the CDF curve of intermediate ARs is in between the simple and complex ARs is unexpected. In the larger F_t regime, the intermediate CDF is more similar to the simple type, i.e., the smaller $K_{int,sim}$ or larger $K_{com,int}$.

3.2. Comparison of Flare Properties in Complex and Simple ARs

In this section, we quantitatively differentiate the flare properties in the complex and simple types of ARs. For a specific lifetime T_{com} and a specific date D_{com}, we first estimate the F_d value by summing up the SXR peak flux of all flare events hosted by the complex ARs with the given T_{com} and D_{com}. The F_d is then normalized to its maximum value among all the derived F_d values. As a result, we obtain one weighted F_d corresponding to its D_{com} for different T_{com}. The same approach is applied to the flaring simple ARs.

The top panel of Figure 3 shows the distribution of weighted F_d values versus T_{com} and D_{com}, where the number at the top of each column indicates the total number of complex ARs with the corresponding T_{com}. It is shown that the majority (>50%) of the studied complex ARs exist for less than four days. In these short-lived complex ARs, most flares occur in the early phase of the complex structure appearance (i.e., smaller D_{com}). When the lifetime becomes longer (e.g., $T_{com} > 7$ days), flares seem to occur at later D_{com}. In comparison, we demonstrate the results of simple ARs in the bottom panel of Figure 3. It is demonstrated that the behaviors are quite different between the flaring simple and complex ARs. More than 80% of the studied simple ARs last for more than four days, and the average lifetime is about eight days, which is roughly twice that of the complex ARs. Our result also indicates higher flare productivity (weighted F_d) in the earlier time of short-lived complex ARs, implying that the short-lived complex ARs would evolve relatively faster than the long-lived complex ARs. However, most of the flares in simple ARs likely occur in the early phase (small D_{sim}) regardless of the lifetime T_{sim}. Therefore, we suggest that the magnetic field configurations in simple ARs are so simple that it is not easy to build up enough magnetic free energy for large flare eruptions even for the long-lived ARs.

Since a complex and long-existing AR is supposed to be the highly potential candidate for hosting intense flares, we analyze the proportion of flare-quiet ARs to those ARs with different T_{com}. Here a complex AR without any flare event larger than B-class is defined as the flare-quiet complex AR. As listed in Table 1, there are 238 ARs in our database classified as complex type during their disk passages, of which 16% are flare-quiet ARs. This percentage varies with lifetime T_{com}, reducing significantly from 38% for the one-day complex ARs to 7% for the ARs with T_{com} longer than one day. Similarly, we apply the same analysis approach to the simple ARs for comparison. We find that 59% of the 4042 simple ARs are flare-quiet, which is much higher than the complex ARs. This percentage decreases from 94% for the one-day simple ARs to 55% for the ARs with T_{sim} longer than one day, which is quite different from the behavior of complex ARs.

3.3. Comparison of Magnetic Properties in Complex and Simple ARs

To differentiate the magnetic characteristics of the complex and simple ARs, we further investigate the photospheric magnetic properties in the complex and simple types of flaring ARs based on the HMI vector magnetograms. Only the flaring ARs located within 30° of the central meridian are considered in order to minimize the projection effects on the calculation of magnetic properties. The magnetograms within two hours before the *GOES* flare start time are selected for the flaring AR events. We also analyze the flare-quiet complex ARs for comparison, where 11 magnetograms with the region of interest near the solar disk center are utilized. In total, there are 506 flares from 53 complex ARs, 463 flares from 192 simple ARs, and 11 flare-quiet complex ARs with available HMI vector magnetograms.

We analyze several magnetic properties of the above ARs. Of special interest are the mean magnetic field strength $\langle B \rangle$, total magnetic flux Φ_t, the flux imbalance Φ_n between opposite magnetic polarities, the field-weighted mean shear angle θ_w, and the source field strength B_s. Here $\langle B \rangle$ and Φ_t are obtained from the strong-field areas where the total field strength is larger than 300 G. Φ_n is estimated from the absolute value of net flux in the areas with $|B_r| > 100$ G. Additionally, the shear angle θ represents the angular deviation of the observed magnetic field from the photospheric potential field; i.e.,

$$\theta = \cos^{-1}\left(\frac{\vec{B}_{obs} \cdot \vec{B}_{pos}}{|\vec{B}_{obs}||\vec{B}_{pos}|}\right),$$

where $\vec{B}_{obs}$ is the magnetic field obtained from the HMI vector magnetogram and $\vec{B}_{pos}$ is the potential field computed from the radial component of $\vec{B}_{obs}$. The θ_w is defined as

$$\theta_w = \frac{\sum \theta |\vec{B}_{obs}|}{\sum |\vec{B}_{obs}|}$$

which is the sum of θ weighted by the local magnetic field over all the pixels in the domain of an HMI magnetogram (Wang et al. 1994). The source field strength B_s is the difference of magnetic field vectors between the observed and potential field in the photosphere (Hagyard et al. 1981); i.e.,

$$B_s = |\vec{B}_{obs} - \vec{B}_{pos}|.$$

We then obtain the mean source field strength $\langle B_s \rangle$ and total source field strength B_{st} in the strong B_s (>800 G) areas.

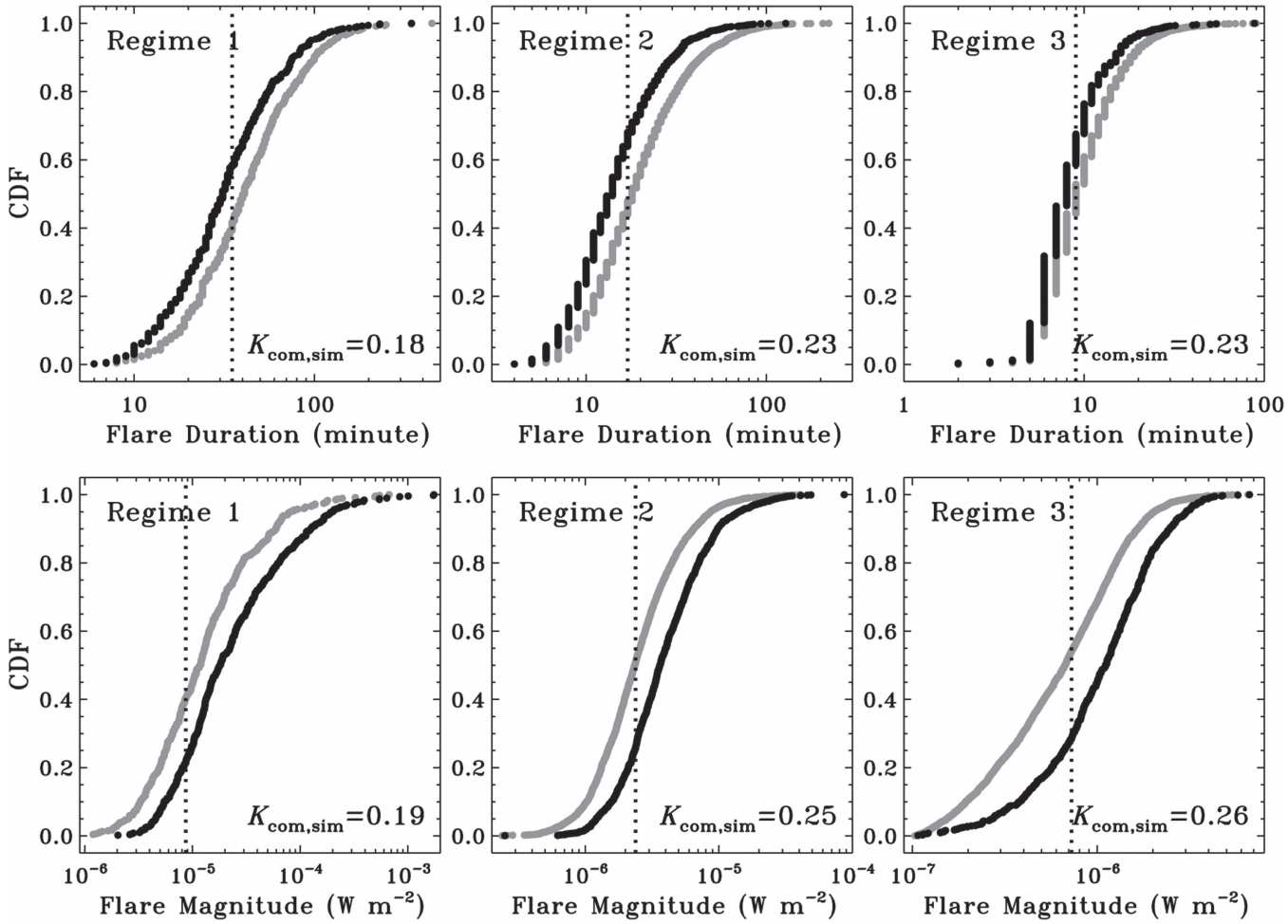

Figure 2. Cumulative distribution function for the flare duration (top panels) and flare magnitude (bottom panels) in different regimes of SXR fluence F_t, where regimes 1, 2, and 3 correspond to $F_t \geqq 10^{-2}$ J m^{-2}, $10^{-3} \leqq F_t < 10^{-2}$ J m^{-2}, and $F_t < 10^{-3}$ J m^{-2}, respectively. The dark and gray curves represent the complex and simple ARs. The vertical dotted line indicates the two-sample KS statistic $K_{com,sim}$.

Figure 4 presents the results of two-sample KS test for the six magnetic quantities mentioned above. Here we only consider the population difference between the complex (dark circle) and simple (gray circle) types of flaring ARs. The vertical dotted line in each plot indicates the location of the corresponding KS statistic $K_{com,sim}$. It is apparent that the values of $\langle B \rangle$, Φ_t, Φ_n, $\langle B_s \rangle$, and B_{st} are larger in the flaring complex ARs than those in the flaring simple ARs. In particular, $\langle B_s \rangle$ and B_{st} (the quantities associated with source field strength) show the significant differences between two CDF curves. We also notice that the smaller θ_w is found in the complex ARs rather than in the simple ARs, which conflicts with the general expectation that the magnetic field configurations in complex ARs would deviate more significantly from the potential field structure compared to those in simple ARs. In addition, it is supposed that the magnetic nonpotentiality is higher in the flaring complex ARs than in the flare-quiet complex ARs. Similarly, Figure 5 demonstrates the CDF comparison for the six parameters between flaring complex (circles) and flare-quiet complex (crosses) ARs with the corresponding KS statistic $K_{com,FQ}$. Among all the analyzed magnetic quantities, B_{st} shows the maximum KS statistic and systematic variation between these two CDFs. Although the data points of the flare-quiet complex are limited, they can still provide insight into the comparison of flaring and flare-quiet complex ARs. The result suggests that B_{st} would be the best among the six physical quantities to differentiate the flare-quiet and flaring complex ARs.

To investigate the dependence of flare magnitude on the magnetic nonpotentiality, Figure 6 displays the total SXR peak flux F_{FL} as a function of $\langle B_s \rangle$ and θ_w (left) as well as a function of B_{st} and θ_w (right) in the complex and simple types of flaring ARs. The F_{FL} is obtained by summing up the SXR peak flux of all flares occurred in the ARs with corresponding $\langle B_s \rangle$ (B_{st}) and θ_w. It is shown that the F_{FL} value in the complex ARs is about 1–2 orders of magnitude larger than that in the simple ARs. We also mark the white cross to represent the flare-quiet complex ARs for a reference. Figure 6 shows that intense flares are preferentially associated with strong-B_{st} rather than high-θ_w regions in the complex ARs. B_{st} likely represents a threshold for determining the flare-quiet and flaring complex ARs. On the contrary, large flares tend to be associated with high-θ_w rather than strong-B_{st} regions in simple ARs. There is no strong correlation of flare magnitude with B_{st} and θ_w in our results.

4. DISCUSSION

It is generally believed that intense flares mainly occur at the regions with complex magnetic field configurations (Low 2015). However, note that not all the ARs with high magnetic complexity associate with intense flares. Table 2 summarizes

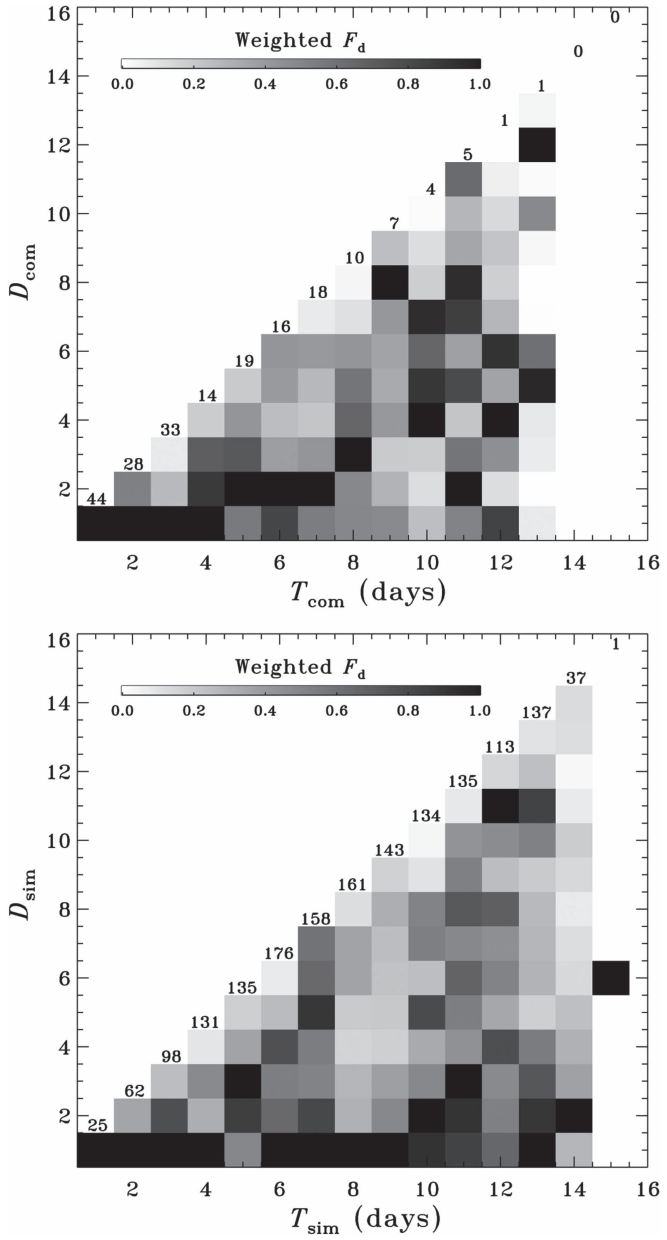

Figure 3. Distribution of the weighted F_d as a function of the lifetime and date of complex ARs (top panel) and simple ARs (bottom panel), where the number above each column denotes the number of total ARs with the corresponding lifetime.

the flare occurrence probability in different types of ARs with the number of flare events and the percentage. It is not surprising that most of the weak flares (69% B-class and 48% C-class) originate from the simple ARs, while most of the strong flares (64% X-class and 41% M-class) erupt from the complex ARs. There is a 64% probability of X-class flare occurrence in highly complex ARs, which is lower than the 95% probability found by Shi & Wang (1994) and 82% found by Sammis et al. (2000). Table 3 lists the flare production rate for each specific type of AR. Since an AR can host many flares with different magnitudes, the ratio of flare event number for a specific magnitude to the total event number is utilized for the estimation in Table 3. For example, if an AR hosts 9 flare events in total during its disk passage, among which 5 events are B-class, 3 events are C-class, and 1 is an M-class flare, the corresponding flare production rate of this AR would be 5/9 for B-, 3/9 for C-, and 1/9 for M-class. Table 3 reveals that the C-class flare is in the majority regardless of the AR magnetic type. Note that there should be more flares below C-class (Christe et al. 2008), which are often not registered in the flare catalog. The complex ARs serve as the most likely potential region for the production of X-class flares compared to other types of ARs, although the probability is much lower than the 40% probability obtained by Sammis et al. (2000). It is inadequate to quantitatively interpret such inconsistencies between different studies because the discrepancy can result from the different data sets, selection criteria, and time coverage of the database. In other words, it is not straightforward to determine an AR capability of intense flare production statistically based on the magnetic classification only.

In addition to the size of a sunspot region, our results suggest that the evolution of magnetic complexity is also important for determining the flare productivity of an AR. In this study, we investigate the flare occurrence date of an AR relative to its AR duration in the complex and simple magnetic types of ARs. The purpose is to characterize the flare productivity in response to the evolution of ARs. Our results reveal that the probability of flare occurrence in the complex ARs increases significantly from 62% to 93% when the lifetime of the $\beta\gamma\delta/\gamma\delta$ configuration increases from one day to longer than one day. We also note that most flares erupting from the long-lived complex ARs tend to occur in the later phase, which is quite different from the long-lived simple ARs. This result is not surprising since magnetic free energy likely builds up for a longer time in order to afford a strong flare. However, even with a long-time evolution, it is difficult for the simple ARs to build up enough magnetic free energy for strong flare eruptions. It is worth mentioning that Guo et al. (2006) analyzed the magnetic field evolution in five ARs using the effective distance as the measure of the complexity of magnetic field configuration. They found that the effective distance is in good correlation with the flare activity, which increases (decreases) in the developing (decaying) δ-type ARs. Nevertheless, insignificant correlation was found in the well-developed δ-type ARs. Their result also suggests that the flare productivity of complex ARs should depend on the evolution stage.

Our results show the tendency for intense flares to erupt from the regions of strong magnetic field, large total flux, or high magnetic nonpotentiality. Tian et al. (2002) and Chen & Wang (2012) investigated the super-ARs, and they found that the ARs with strong flux imbalance, greater than 10^{21} Mx, can produce more intense flares. In our study, we found that not only the flaring complex ARs, but also the flaring simple ARs, have such a high flux imbalance between opposite magnetic polarities. However, only 2% of the flaring simple ARs have an imbalanced flux greater than 10^{22} Mx. This percentage is much lower than the 17% probability in flaring complex ARs. Note that since the flux imbalance derived here is from the whole flaring AR on the basis of preflare magnetograms with a 720 s cadence, our results cannot display the rapid evolution of magnetic structure at localized regions. The emergence or submergence of magnetic flux across the photosphere or the cancellation of the emerged magnetic field with surrounding field might lead to a flare, although this is not defined in this study.

Table 1
AR Capability of Flare Production for Different Lifetimes of Magnetic Complexity

	Complex ARs			Simple ARs		
	Flaring	Flare-quiet	Total	Flaring	Flare-quiet	Total
$T_i = 1$ day	44 (62%)	27 (38%)	71 (100%)	25 (6%)	383 (94%)	408 (100%)
$T_i > 1$ day	156 (93%)	11 (7%)	167 (100%)	1621 (45%)	2013 (55%)	3634 (100%)
Total	200 (84%)	38 (16%)	238 (100%)	1646 (41%)	2396 (59%)	4042 (100%)

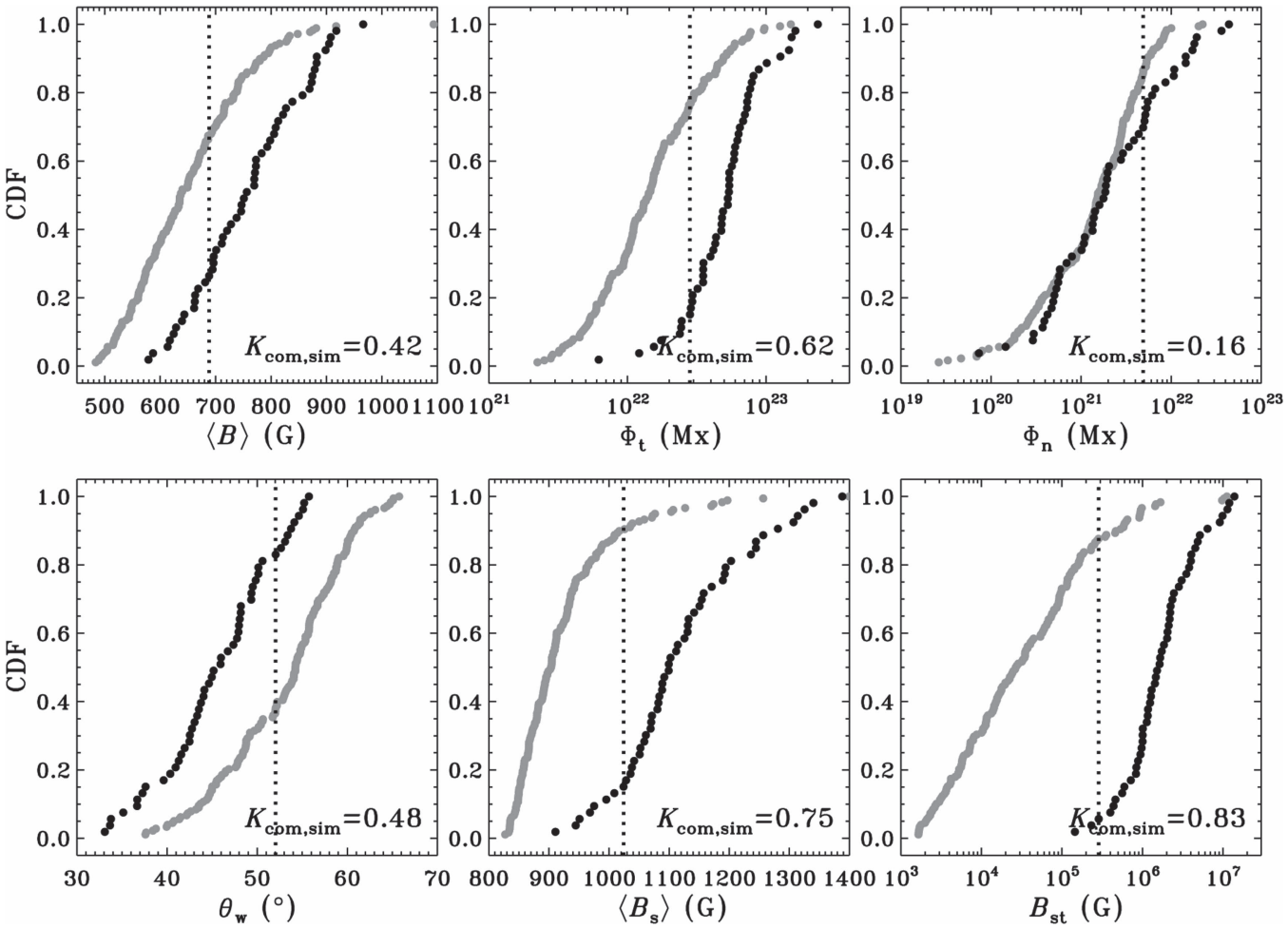

Figure 4. Cumulative distribution function for the mean magnetic field strength $\langle B \rangle$, total magnetic flux Φ_t, the flux imbalance Φ_n between opposite magnetic polarities, the field-weighted mean shear angle θ_w, the mean source field strength $\langle B_s \rangle$, and total source field strength B_{st} in the flaring complex (dark) and simple (gray) ARs. The vertical dotted line in each plot indicates the corresponding KS statistic $K_{com,sim}$.

To clarify the dependence of AR magnetic properties on flare activity, Figure 7 demonstrates the association of integrated SXR peak flux F_{AR} with six magnetic quantities in the complex (dark circles) and simple (gray circles) ARs. The Spearman's rank correlation is used to derive the correlation coefficient, as indicated in the top of each plot. It is found that the quantities in association with strong field area (Φ_t) or source field strength ($\langle B_s \rangle$ and B_{st}) have a higher correlation with F_{AR}. In particular, B_{st} in the complex ARs has the highest correlation ($\sim$0.8) with F_{AR}, which seems to be the key parameter related to the flare activity. Additionally, Φ_n in the complex ARs has the lowest correlation with flare activity and θ_w shows a negative correlation with F_{AR}. We thus suggest that B_{st} can be regarded as a good indicator of photospheric magnetic free energy, i.e., more directly related to the flare occurrence. Another quantities, Φ_n or θ_w, would be appropriate for describing the overall AR properties rather than determining the productivity of intense flares.

In addition, we perform principal component analysis to identify the maximum variance of event data as well as the contribution of each magnetic variable (Feigelson & Babu 2012). The six variables used for the analysis are $\langle B \rangle$, $\log(\Phi_t)$, $\log(\Phi_n)$, θ_w, $\langle B_s \rangle$, and $\log(B_{st})$. Here the principal components are derived from the covariance matrix of modified event data by subtracting the mean of each variable and normalizing to its maximum. Figure 8(a) demonstrates the scree graph for eigenvalues of the modified event data. It is suggested that the first two principal components with the larger eigenvalues should be retained. The derived first two principal components, PC1 and PC2, are given as

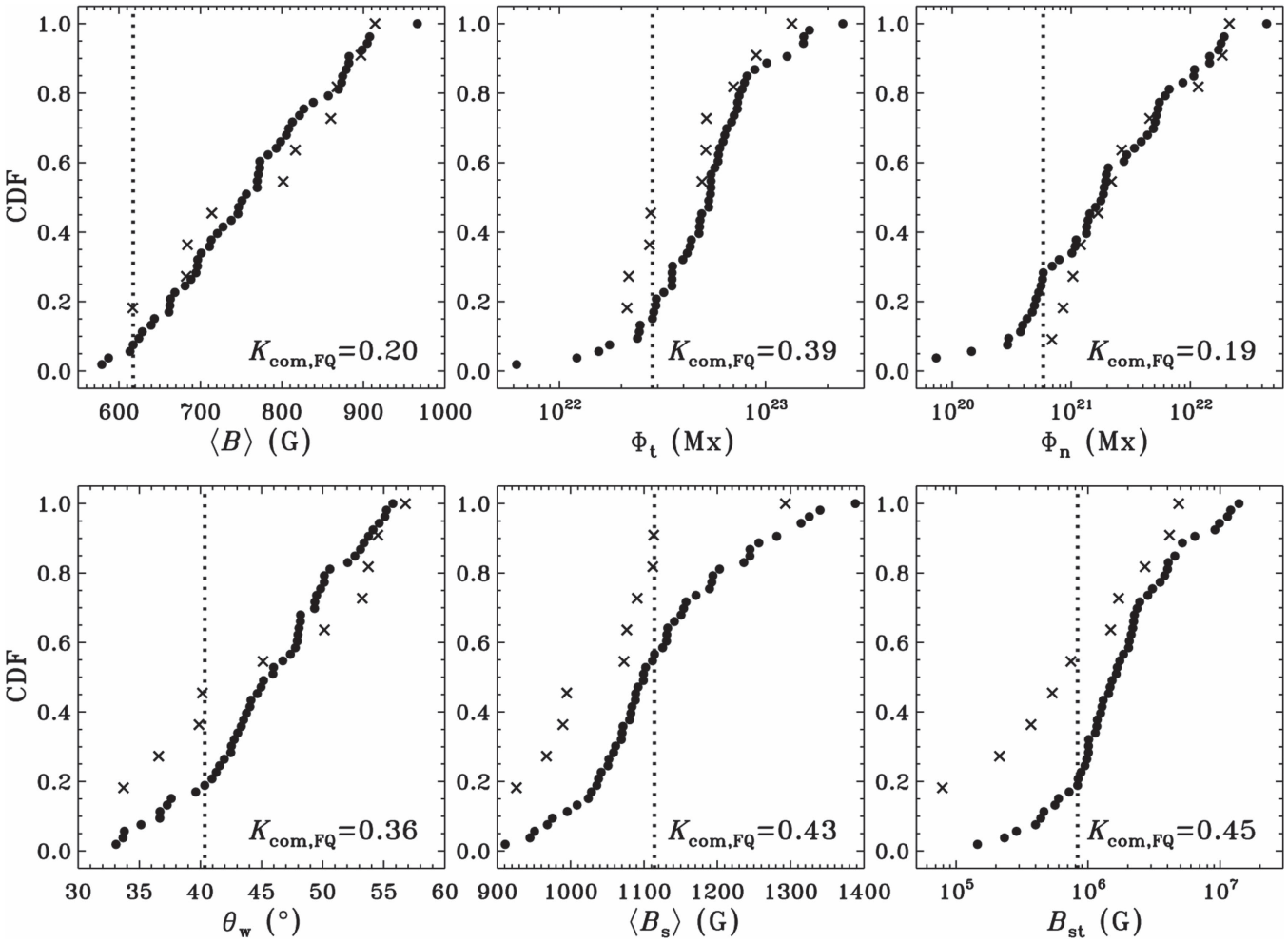

Figure 5. Same as Figure 4 but for flaring complex (circles) and flare-quiet complex (crosses) ARs. The vertical dotted line indicates the KS statistic $K_{com,FQ}$.

follows:

$$\begin{aligned} PC1 = {} & 0.393(\langle B \rangle) + 0.068(\log(\Phi_t)) + 0.020(\log(\Phi_n)) \\ & - 0.457(\theta_w) + 0.389(\langle B_s \rangle) + 0.695(\log(B_{st})) \end{aligned} \quad (1)$$

$$\begin{aligned} PC2 = {} & 0.547(\langle B \rangle) - 0.035(\log(\Phi_t)) - 0.052(\log(\Phi_n)) \\ & - 0.580(\theta_w) - 0.277(\langle B_s \rangle) - 0.532(\log(B_{st})). \end{aligned} \quad (2)$$

Note that all six variables have been normalized to the values between 0 and 1.

Figure 8(b) demonstrates the first two components for the modified event data, where the dark circles, triangles, and gray circles denote the flaring complex, flare-quiet complex, and flaring simple ARs, respectively. Since the first two components account for 91% of the total variance, Figure 8(b) can represent the event data without many distortions. The plots of the first and third principal components (Figure 8(c)) as well as the second and third components (Figure 8(d)) are shown for comparison. As expected, the data have the largest variance in the first principal component. It is also found that the flaring complex ARs are mainly located at the positive side of the first principal component, while most of the flaring simple ARs are located at the negative side. This can be explained by the contributions of B_{st} and θ_w as well as their different properties in the complex and simple types of flaring ARs. As given in Equation (1), PC1 has its major and positive contribution from $\log(B_{st})$ together with a secondary but negative contribution from θ_w. The combination of larger B_{st} and smaller θ_w in flaring complex ARs results in a positive value of PC1, while the combination of larger θ_w and smaller B_{st} in flaring simple ARs leads to a negative value of PC1. Note that the result of the principal component analysis supports our Figure 7: B_{st} and θ_w can be utilized to differentiate the complex and simple types of flaring ARs. However, it is difficult to distinguish between flaring and flare-quiet complex ARs from the principal component analysis.

To demonstrate the temporal evolutions of the magnetic properties in different ARs, Figure 9 illustrates the variations of the derived magnetic parameters from the flaring simple AR 11281 (left), flaring complex AR 11890 (middle), and flare-quiet complex AR 12109 (right), as well as the *GOES* SXR light curves. The magnetic quantities are obtained from the magnetograms with the AR around the central meridian to minimize the calculation uncertainty due to projection effect. Namely, AR 11281 moves from S20E28 to S19W24 during 2011 September 1–5, AR 11890 moves from S11E36 to S12W28 during 2013 November 6–11, and AR 12109 moves from S08E36 to S07W32 during 2014 July 6–11. The vertical dotted lines indicate the flare events associated with the specific AR. Note that only those flares larger than M-class (C-class)

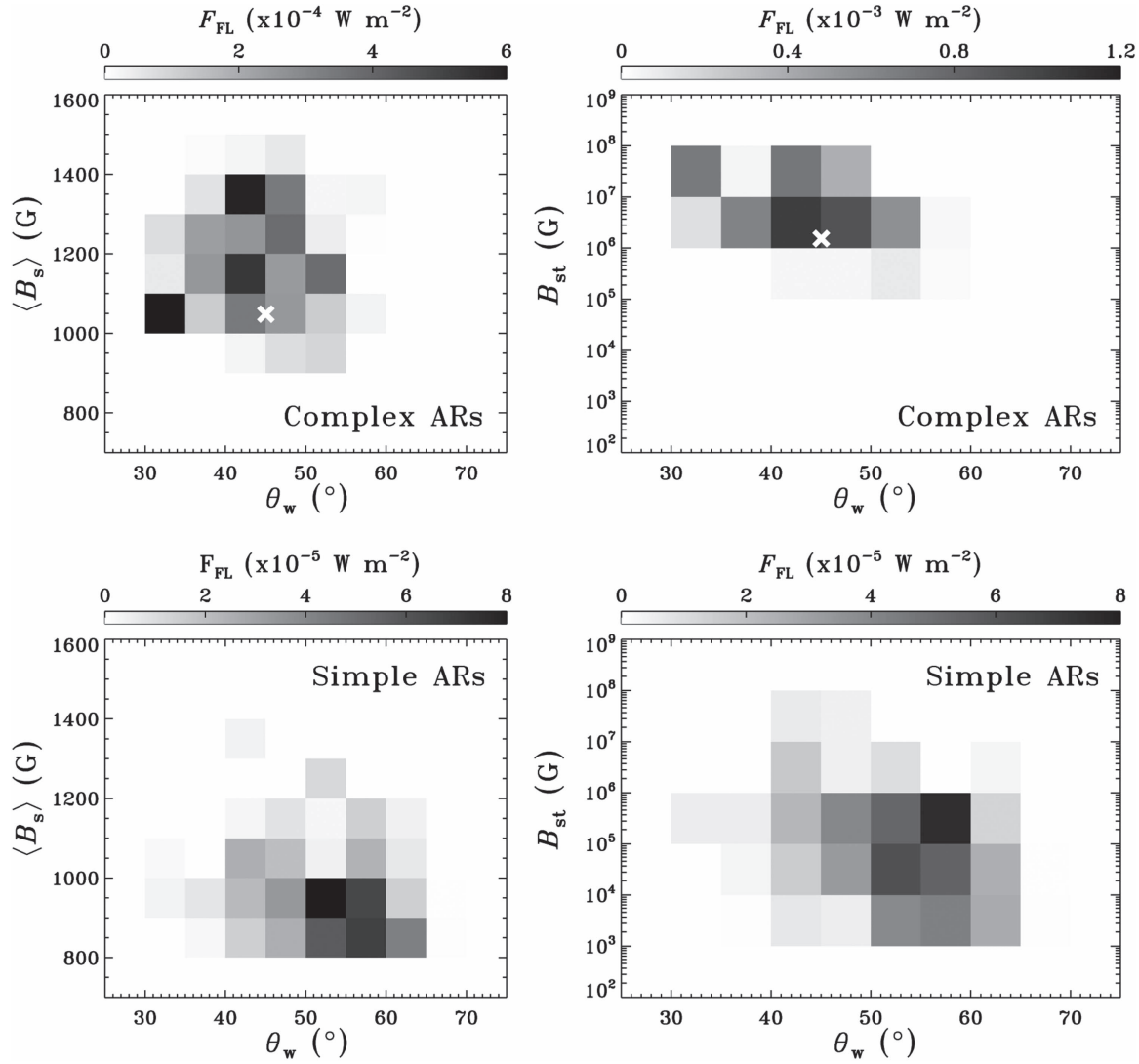

Figure 6. (Left) Total SXR peak flux F_{FL} as a function of $\langle B_s \rangle$ and θ_w in flaring complex (top panel) and flaring simple (bottom panel) ARs. (Right) F_{FL} as a function of B_{st} and θ_w in flaring complex (top panel) and flaring simple (bottom panel) ARs. The white cross in the top panel represents the flare-quiet complex ARs for reference.

Table 2
Summary of Flare Probability for Different Types of ARs

	Simple ARs	Intermediate ARs	Complex ARs	Total
B-class Flares	2871 (69.2%)	910 (21.9%)	368 (8.9%)	4149 (100%)
C-class Flares	4078 (47.5%)	2678 (31.2%)	1822 (21.3%)	8578 (100%)
M-class Flares	352 (32.5%)	290 (26.8%)	440 (40.7%)	1082 (100%)
X-class Flares	20 (18.9%)	18 (17.0%)	68 (64.1%)	106 (100%)
Total	7321	3896	2698	13915

Table 3
Summary of Production Rate for Different Magnitude Flares

	B-class Flares	C-class Flares	M-class Flares	X-class Flares	Total
Simple ARs	527.96 (32.1%)	1027.35 (62.4%)	84.32 (5.1%)	6.37 (0.4%)	1646 (100%)
Intermediate ARs	118.32 (21.4%)	392.09 (70.9%)	39.29 (7.1%)	3.30 (0.6%)	553 (100%)
Complex ARs	30.75 (15.4%)	135.34 (67.7%)	27.35 (13.7%)	6.56 (3.2%)	200 (100%)
Total	677.03	1554.78	150.96	16.23	2399

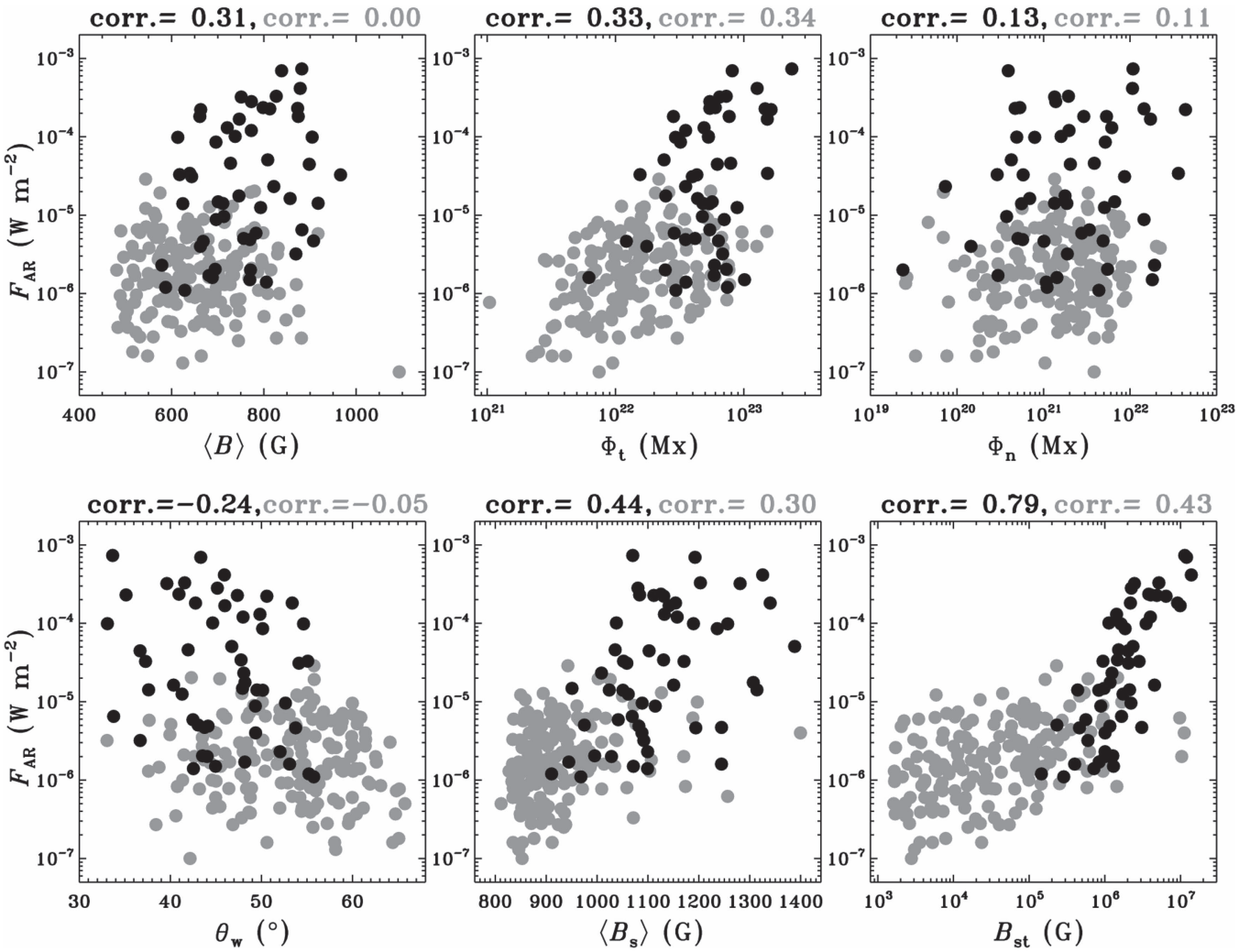

Figure 7. Scatter plots of integrated SXR peak flux F_{AR} verse six magnetic quantities in the complex (dark circle) and simple (gray circle) ARs with the corresponding coefficient of Spearman's rank correlation.

are denoted for the complex (simple) AR. Besides the flux imbalance Φ_n, the absolute values of total magnetic flux from the negative (positive) polarity Φ_- (Φ_+) with $|B_r| > 100$ G are also shown as the gray (dashed) curve in the fourth panel. The large variations of Φ_n seen in AR 11890 on 2013 November 8 and 9 as well as in AR 12109 on 2014 July 6 result from the relatively large decrease in Φ_-, which could be indicative of the flux submergence across the photosphere. Among all the parameters in these three ARs, the mean source field strength $\langle B_s \rangle$ in AR 11890 apparently has the most evident coincidence with the intense flares. It increases before the flares and then decreases after the flares, which is consistent with the storage and release of magnetic free energy for the flare occurrence. However, there is no such correspondence found in the simple AR 11281. It is noted that no intense flare occurs on 2013 November 9 even though $\langle B_s \rangle$ reaches peaks as well. The decreasing trend of total source field strength B_{st} in AR 11890 could indicate the successive release of magnetic free energy due to the consecutive eruptions of intense flares. The lack of one-to-one temporal correspondence between $\langle B_s \rangle$ (B_{st}) change and flare activity in the case study implies that there should be other factors related to the triggering of solar flares, such as the morphology of coronal magnetic fields or the magnetic field connections with surrounding ARs, rather than photospheric parameters alone.

We notice that B_{st} derived here is similar to the proxy of photospheric excess energy defined by Su et al. (2014). Su et al. (2014) investigated the relationship between flare index and several magnetic parameters in 61 ARs based on the HMI vector magnetograms and model extrapolations. Their results showed the highest correlation (∼63%) between the flare index and the photospheric excess energy, which is computed only at the photospheric surface. In our results, the strong B_{st} with an intermediate θ_w in flaring complex ARs implies that the magnetic free energy provided by a complex AR is large enough to trigger a flare eruption before the photospheric magnetic shear becomes too large. In other words, high magnetic shear would be a required condition for triggering a flare at the region with low magnetic free energy. Note that the coronal magnetic fields are not taken into account in our calculations, which could result in the underestimation of magnetic nonpotentiality in the entire flaring ARs, especially for the complex type. In a word, our study suggest that the total source field strength B_{st} would be a considerable parameter for

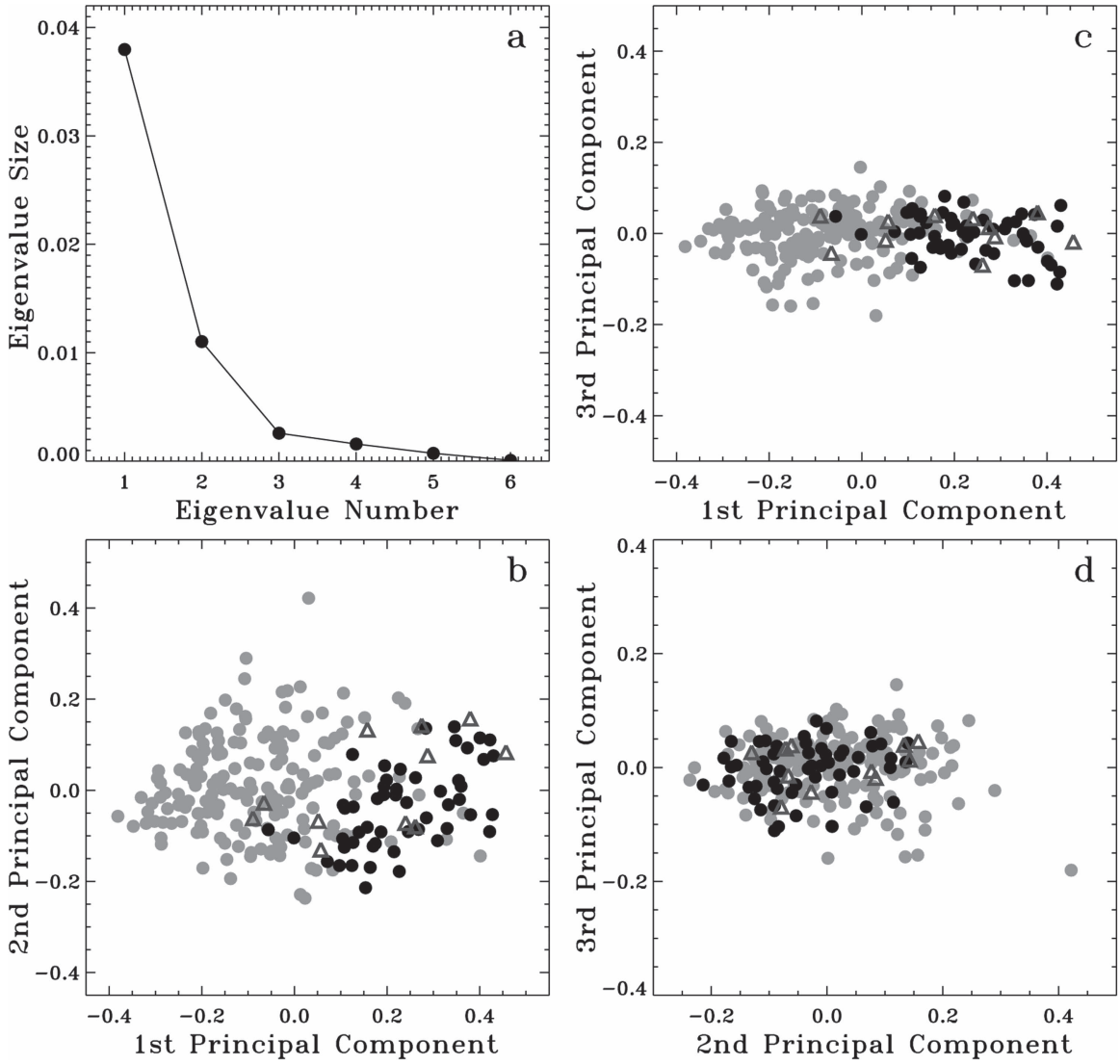

Figure 8. (a) A scree graph for eigenvalues of the data is shown in the top-left panel. (b)–(d) Plots of principal components for the modified flare event data, where the dark circles, triangles, and gray circles correspond to the flaring complex, flare-quiet complex, and flaring simple ARs, respectively.

examining the flare productivity of an AR when one only considers the photospheric magnetic field data.

5. CONCLUSION

On the basis of two data sets of daily sunspot and flare information, we statistically study the dependence of flare productivity on the AR properties using *GOES* SXR measurements during 1996–2014. All the analyzed ARs are classified as simple, intermediate, and complex types according to the magnetic complexity suggested by Mount Wilson sunspot classification. Of special interest is the comparison of magnetic properties relative to flare eruptions between the complex and simple types of ARs.

We investigate several photospheric magnetic parameters such as the mean magnetic field strength, total magnetic flux, flux imbalance, field-weighted mean shear, and source field strength based on the HMI vector magnetograms during the period 2010–2014. Our results show good agreement with previous studies that intense flares preferentially occur at the large-size ARs with strong magnetic fields and complex field configurations. In addition, we demonstrate the importance of considering the lifetime of an AR with the highest magnetic complexity when one determines the flare productivity of an AR. Our result indicates that the higher flare productivity occurs at the earlier phase of short-lived complex ARs. For the long-lived complex ARs, the major flares tend to occur in the later phase of the $\beta\gamma\delta/\gamma\delta$ appearance. Similar to previous studies, we find that complex ARs are highly potential regions for the production of X-class flares. Moreover, the flares originating from complex ARs are often more intense and impulsive.

Among all the investigated magnetic properties, our study suggests that the total source field strength (B_{st}) has the best correlation with the flare activity, especially for the complex ARs. The total source field strength can be regarded as the proxy of photospheric magnetic free energy, likely serving as the lowest threshold for the strong flare eruptions in the complex ARs. Therefore, we conclude that the magnetic free energy rather than the magnetic field complexity in the photosphere is the primary parameter associated with the flare

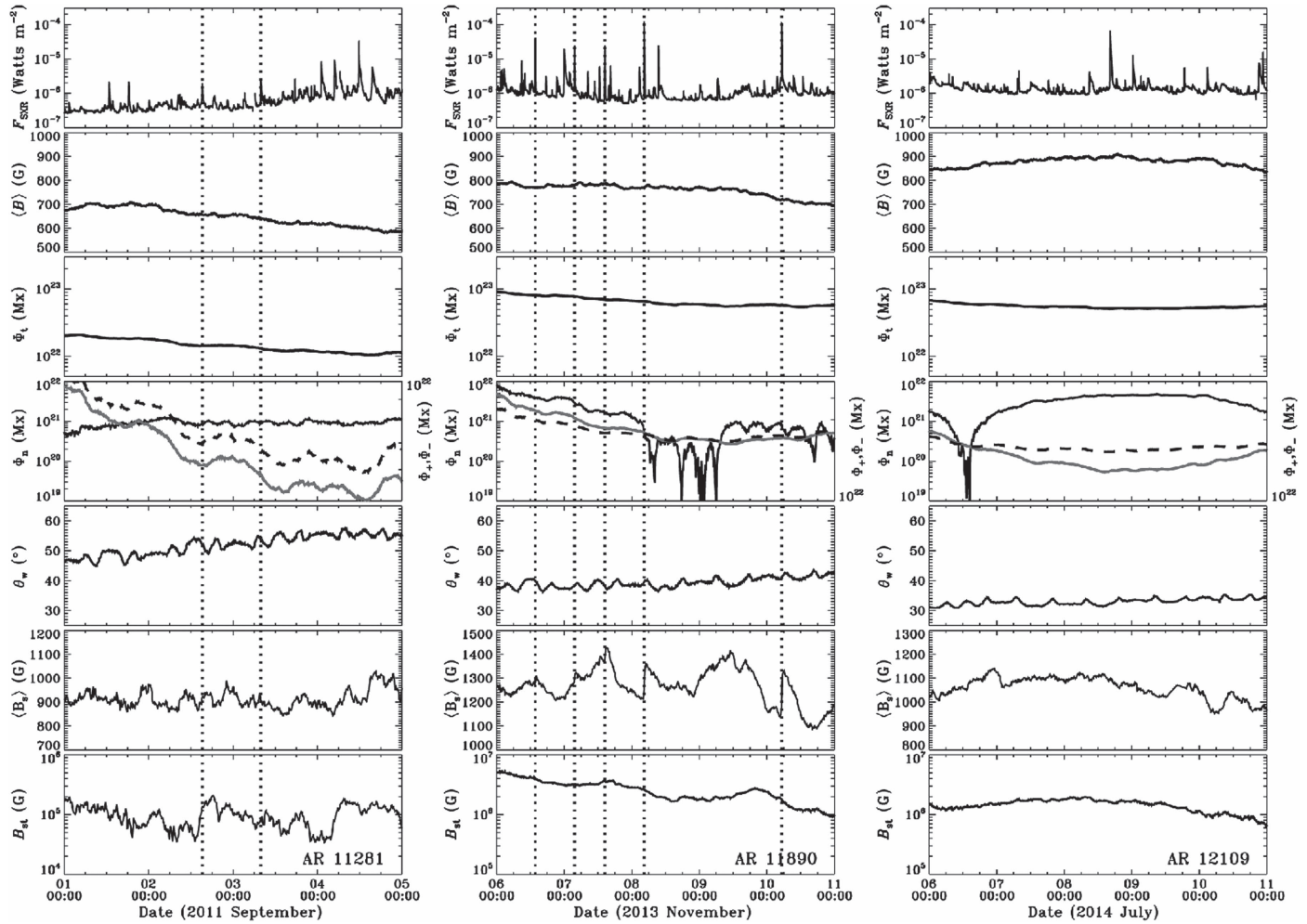

Figure 9. Illustration of the *GOES* SXR light curves and the temporal variations of derived magnetic parameters from the flaring simple AR 11281 (left), flaring complex AR 11890 (middle), and flare-quiet complex AR 12109 (right). Here the vertical dotted lines indicate the flare events associated with the specific AR. Note that only the flares larger than M-class (C-class) are denoted for the complex (simple) AR. The gray (dashed) curve in the fourth panel represents the absolute value of total magnetic flux from the negative (positive) polarity Φ_- (Φ_+) with $|B_r| > 100$ G.

productivity of an AR, especially for the occurrence of intense flares.

We are grateful to the *GOES* and *SDO*/HMI teams for providing the data sets. Y.H.Y. also thanks Dr. Xudong Sun for help with the HMI SHARP data series. This work is supported by the Ministry of Science and Technology of the R.O.C. under grant MOST 104-2111-M-008-017. P.F.C. is supported by the grants NSFC (11533005 and 11025314) and Jiangsu 333 Project.

REFERENCES

Atac, T. 1987, Ap&SS, 129, 203
Bobra, M. G., Sun, X., Hoeksema, J. T., et al. 2014, SoPh, 289, 3549
Chen, A. Q., & Wang, J. X. 2012, A&A, 543, 49
Chen, A. Q., Wang, J. X., Li, J. W., Feynman, J., & Zhang, J. 2011, A&A, 534, 47
Christe, S., Hannah, I. G., Krucker, S., McTiernan, J., & Lin, R. P. 2008, ApJ, 677, 1385
Cui, Y., Li, R., Wang, H., & He, H. 2007, SoPh, 242, 1
Feigelson, E. D., & Babu, G. J. 2012, Modern Statistical Methods for Astronomy with R Applications (Cambridge: Cambridge Univ. Press)
Giovanelli, R. G. 1939, ApJ, 89, 555
Greatrix, G. R. 1963, MNRAS, 126, 132
Guo, J., Lin, J., & Deng, Y. 2014, MNRAS, 441, 2208
Guo, J., Zhang, H., Chumak, O. V., & Lin, J. 2006, SoPh, 237, 25
Hagyard, M. J., Teuber, D., West, E. A., & Smith, J. B. 1984, SoPh, 91, 115
Hagyard, M., Low, B. C., & Tandberg-Hanssen, E. 1981, SoPh, 73, 257
He, H., Wang, H., Yan, Y., Chen, P. F., & Fang, C. 2014, JGRA, 119, 3286
Jing, J., Tan, C., Yuan, Y., et al. 2010, ApJ, 713, 440
Lee, K., Moon, Y.-J., Lee, J.-Y., Lee, K.-S., & Na, H. 2012, SoPh, 281, 639
Leka, K. D., & Barnes, G. 2003, ApJ, 595, 1296
Leka, K. D., & Barnes, G. 2007, ApJ, 656, 1173
Low, B. C. 2015, SCPMA, 58, 15201
Mayfield, E. B., & Lawrence, K. L. 1985, SoPh, 96, 293
Romano, P., & Zuccarello, F. 2007, A&A, 474, 633
Sammis, I., Tang, F., & Zirin, H. 2000, ApJ, 540, 583
Scherrer, P. H., Schou, J., Bush, R. I., et al. 2012, SoPh, 275, 207
Schou, J., Scherrer, P. H., Bush, R. I., et al. 2012, SoPh, 275, 229
Shi, Z. X., & Wang, J. X. 1994, SoPh, 149, 105
Su, J. T., Jing, J., Wang, S., Wiegelmann, T., & Wang, H. 2014, ApJ, 788, 150
Sun, X. 2013, arXiv:1309.2392S (http://arxiv.org/abs/1309.2392)
Takizawa, K., & Kitai, R. 2015, SoPh, 290, 2093
Tian, L., Liu, Y., & Wang, J. 2002, SoPh, 209, 361
Tiwari, S. K., Venkatakrishnan, P., & Gosain, S. 2010, ApJ, 721, 622
Wang, H., Ewell, M. W., Jr., Zirin, H., & Ai, G. 1994, ApJ, 424, 436
Wang, J., Shi, Z., Wang, H., & Lue, Y. 1996, ApJ, 456, 861
Yang, X., Zhang, H. Q., Gao, Y., Guo, J., & Lin, G. H. 2012, SoPh, 280, 165
Yang, Y.-H., Chen, P. F., Hsieh, M.-S., et al. 2014, ApJ, 786, 72
Zirin, H., & Liggett, M. A. 1987, SoPh, 113, 267